

The distribution of ionized, atomic and PDR gas around S 1 in ρ Ophiuchus

B. Mookerjea¹, G. Sandell², V. S. Veena³, R. Güsten⁴, D. Riquelme⁴, H. Wiesemeyer⁴, F. Wyrowski⁴, and M. Mertens³

¹ Tata Institute of Fundamental Research, Homi Bhabha Road, Mumbai 400005, India e-mail: bhaswati@tifr.res.in

² Institute for Astronomy, University of Hawaii, 640 N. Aohoku Place, Hilo, HI 96720, USA

³ I. Physikalisches Institut, Universität zu Köln, Zùlpicher Str. 77, D-50937 Köln, Germany

⁴ Max Planck Institut für Radioastronomie, Auf dem Hügel 69, D-53121 Bonn, Germany

latest revision February 23, 2021

ABSTRACT

The early B star S 1 in the ρ Ophiuchus cloud excites an H II region and illuminates a large egg-shaped photodissociation (PDR) cavity. The PDR is restricted to the west and south-west by the dense molecular ρ Oph A ridge, expanding more freely into the diffuse low density cloud to the north-east. We analyze new SOFIA GREAT, GMRT and APEX data together with archival data from Herschel/PACS, JCMT/HARPS to study the properties of the photo-irradiated ionized and neutral gas in this region. The tracers include [C II] at $158\ \mu\text{m}$, [O I] at 63 and $145\ \mu\text{m}$, $J=6-5$ transitions of CO and ^{13}CO , $\text{HCO}^+(4-3)$, radio continuum at 610 and 1420 MHz and H I at 21 cm. The PDR emission is strongly red-shifted to the south-east of the nebula, and primarily blue-shifted on the north western side. The [C II] and [O I]63 spectra are strongly self-absorbed over most of the PDR. By using the optically thin counterparts, [$^{13}\text{C II}$] and [O I]145 respectively, we conclude that the self-absorption is dominated by the warm (> 80 K) foreground PDR gas and not by the surrounding cold molecular cloud. We estimate the column densities of C^+ and O^0 of the PDR to be $\sim 3 \times 10^{18}$ and $\sim 2 \times 10^{19}\ \text{cm}^{-2}$, respectively. Comparison of stellar far-ultraviolet flux and reprocessed infrared radiation suggest enhanced clumpiness of the gas to the north-west. Analysis of the emission from the PDR gas suggests the presence of at least three density components consisting of high density ($10^6\ \text{cm}^{-3}$) clumps, medium density ($10^4\ \text{cm}^{-3}$) and diffuse ($10^3\ \text{cm}^{-3}$) interclump medium. The medium density component primarily contributes to the thermal pressure of the PDR gas which is in pressure equilibrium with the molecular cloud to the west. Emission velocities in the region suggest that the PDR is tilted and somewhat warped with the south-eastern side of the cavity being denser on the front and the north-western side being denser on the rear.

Key words. ISM: Clouds – Submillimeter: ISM – ISM: lines and bands –(ISM:) photon-dominated region (PDR) –ISM: individual (ρ Oph)

1. Introduction

Photon-dominated Regions (PDRs) are regions where far-ultraviolet (FUV) ($6\ \text{eV} < h\nu < 13.6\ \text{eV}$) radiation from young massive stars dominate the physics and the chemistry of the interstellar medium (Tielens & Hollenbach 1985). The PDRs play an important role in reprocessing much of the energy from stars and re-emitting this energy in the infrared-millimeter regime. Most of the mass of the gas and dust in the Galaxy resides in PDRs (Hollenbach & Tielens 1999). In the far infrared the most important cooling lines are the fine structure lines of [C II] at $158\ \mu\text{m}$, and [O I] at 63 & $145\ \mu\text{m}$ and to a lesser extent high- J CO lines, while PAH emission and H_2 lines dominate in the near- and mid-IR. Of these tracers [C II] being the most abundant and easily excited is the most ubiquitous. Owing to an ionization potential of 11.26 eV for Carbon, understanding the phase of gas from which [C II] arises requires comparison with bona-fide tracers of ionized, atomic and molecular gas.

Mookerjea et al. (2018) recently published an observational study of the [C II] emission from a region around the B4V star S 1 located in the ρ Ophiuchus dark cloud (Ortiz-León et al. 2017, at a distance of 137.3 ± 1.2 pc). The S 1 PDR is located on the eastern edge of the westernmost core ρ Oph A (Loren, Wootten & Wilking 1990). The ρ Oph A core has a filamentary structure with at least nine pre- and protostellar cores (Wilson et al. 1999; Di Francesco, André & Myers 2004), includ-

ing the prototypical Class 0 source VLA 1623. Most of the cores are starless, although two of the cores may have embedded proto-stars (Friesen et al. 2018; Kawabe et al. 2018). Mookerjea et al. (2018) found that the [C II] emission is dominated by the strong emission from the nebula surrounding S 1 that appears to expand into the dense Oph A molecular cloud to the west and south of S 1. The [C II] emission is distributed similar to the other PDR tracers such as the $8\ \mu\text{m}$ continuum tracing emission from PAHs and the velocity-integrated emission of [O I] at 145 and $63\ \mu\text{m}$ measured by Larsson & Liseau (2017). A comparison of [C II] with the $J=3-2$ emission of CO and ^{13}CO shows very little similarity, although the highly compressed parts of the PDR shell traced by [C II] show up in $\text{C}^{18}\text{O}(3-2)$ as well as $\text{HCO}^+(4-3)$. Mookerjea et al. (2018) also detected [C II] to be strongly self-absorbed over an extended region in the S 1 PDR and interpreted it as a cold foreground cloud being absorbed against the warm background gas. Analysing velocity-unresolved Herschel/PACS data, Larsson & Liseau (2017) deduced that this cold foreground cloud absorbs most of the $^3\text{P}_1-^3\text{P}_2$ [O I] $63\ \mu\text{m}$ radiation but leaves the higher level $^3\text{P}_0-^3\text{P}_1$ [O I] $145\ \mu\text{m}$ line unaffected.

In this paper we present newly observed maps of radio continuum, H I at 21 cm, [C II] at $158\ \mu\text{m}$, [O I] at 63 and $145\ \mu\text{m}$ and $J=6-5$ transitions of CO and ^{13}CO and use them to study the morphology and physical properties of the PDR around the star S 1.

2. Observations & Data Reduction

2.1. SOFIA

The S 1 PDR was observed on two occasions on June 14, 2018 and June 5, 2019 with upGREAT¹ (Risacher et al. 2018) on flights leaving from Christchurch, New Zealand. All observations were done in Consortium time (Project 83_0614). The bright PDR was mapped simultaneously in both oxygen fine-structure lines: the HFA array was tuned to [O I] 63 μm ($f = 4744.77749$ GHz), while the LFA-H polarization sub-array was tuned to [O I] 145 μm ($f = 2060.06886$ GHz). The mapped field, indicated in Fig.4, was sampled at 3'' spacing, with 0.4 sec integration time per dump. In order to record the extended, lower-level PDR emission, in 2019 a wider field of 294'' \times 294'' centered on S 1, was added with the LFA tuned to [C II] 158 μm sampling every 6'' at a scan rate of 0.4 sec per resolution element. All mapping was carried-out under dry atmospheric conditions at 42,000–43,000 ft flight altitude in total power on-the-fly mode, with the reference position at -120'', +300'' relative to S 1. The off position was clean for [O I], but there was still [C II] emission in the off position. We therefore took a longer single pointed observation toward this off against a far off position (offset at 833'', -167''), which allowed us to correct the [C II] map for the contamination in the (near) off position. The spectrometer setting during the [C II] observation also covered the strongest hyperfine transition (2–1; 1900.4661 Hz) of the [¹³C II].

The observations were reduced and calibrated by the GREAT team. The GREAT team also provided beam sizes (14''1 for [C II], 13'' for [O I]145 and 6''3 for [O I]63) and beam efficiencies derived from planet observations. The data were corrected for atmospheric extinction and calibrated in T_{mb} . In June 2018 the telluric 63 μm [O I] line was at $V_{lsr} = 1.6 \text{ km s}^{-1}$, essentially making the 63 micron data unusable. In June 2019 the S 1 PDR was observed earlier in the month shifting the telluric 63 μm [O I] to 7.5 km s^{-1} , well away from the emission from the PDR except for some of the red-shifted [O I] spectra in the southern part of the PDR cavity. Comparison with the 2018 data which were clean at these velocities, show that very few spectra in the 2019 data are affected. Further processing of the data (conversion to main-beam brightness temperature, with beam efficiencies of 0.58, and averaging with $1/\sigma^2$ rms weighting) was made with the CLASS² software. The final maps of [C II] and [O I] 63 and 145 μm presented here are centered at 16:26:34.175 - 24:23:28.3 (J2000), which corresponds to the position of the star S 1.

2.2. Radio observations with GMRT

We have mapped the low frequency radio continuum emission and 21 cm H I emission towards ρ Ophiuchus using the upgraded Giant Metrewave Radio Telescope (uGMRT; Gupta et al. 2017), India. The GMRT interferometer comprises of 30 antennae, each of diameter 45 m that are arranged in a Y-shaped configuration (Swarup et al. 1991). Of these, twelve antennae are located randomly within a central region of area $1 \times 1 \text{ km}^2$ and the remaining eighteen antennae are placed along three arms, each of length 14 km. The shortest and longest baselines are 105 m and 25 km

¹ The German REceiver for Astronomy at Terahertz frequencies (upGREAT) is a development by the MPI für Radioastronomie and the KOSMA/Universität zu Köln, in cooperation with the DLR Institut für Optische Sensorsysteme.

² CLASS is part of the GILDAS software package, see <http://www.iram.fr/IRAMFR/GILDAS>

Table 1. Details of the radio observations with GMRT.

Frequency (MHz)	610		1420	
	Continuum		Line	
Observation date	10 July 2018	12, 13 July 2018	12, 13 July 2018	12, 13 July 2018
On source time (hrs)	3.9	14.7	14.7	14.7
Bandwidth (MHz)	32	32	32	12.5
Primary Beam	45'.8	19'.7	19'.7	19'.7
Synthesized beam	7''.0 \times 4''.8	5''.8 \times 3''.2	5''.8 \times 3''.2	21''.3 \times 14''.3 ^a
Position angle (°)	-5.4	30.9	30.9	14.9
Noise (mJy beam ⁻¹)	1.5	0.6	0.6	4.5

^a Medium resolution opted to ensure detection of the emission with high fidelity in the channel maps

respectively. The configuration enables us to map large and small scale structures simultaneously. The observations were carried out during July 2018. The radio source 3C286 was used as the primary flux calibrator and bandpass calibrator whereas 1626-298 was used as phase calibrator.

The observed field was centered at ρ Ophiuchus (α_{J2000} : 16^h26^m34.0^s, δ_{J2000} : -24°23'28.0''). The radio continuum observations were carried out at 610 and 1420 MHz. The angular sizes of the largest structure observable with GMRT are 17' and 7' at 610 and 1420 MHz, respectively. H I observations were carried out along with the 1420 MHz radio continuum observations. The rest frequency of H I line is 1420.4057 MHz. The H I observations were performed with a bandwidth of 12.5 MHz, which was further divided into 8192 channels. The observing frequency was estimated considering the LSR velocity of 3 km s^{-1} (Pankonin & Walmsley 1978) as well as motions of the Earth and the Sun. The settings correspond to a spectral resolution of 1.526 kHz (velocity resolution of 0.322 km/s).

The data reduction was carried out using the NRAO Astronomical Image Processing System (AIPS). The data sets were carefully checked and corrupted data due to radio frequency interference, non-working antennas, bad baselines etc. were flagged. After thorough flagging, the data was flux and phase calibrated using the calibrators 3C286 and 1626-298. The data sets were cleaned and deconvolved to create continuum maps. Several iterations of self-calibration were applied to minimize the phase errors. The final images were then primary beam corrected.

There are two sets of H I observations: one on July 12 and the other one on July 13, 2018. For the H I observations, each of the final calibrated data set was cleaned and deconvolved to produce a continuum map. Next, we subtracted the continuum (created from the line free channels). The two data sets were then combined together to increase the signal-to-noise ratio. We imaged the source with a UV tapering of 10 k λ and a spectral cube was generated. The primary beam correction was applied and the final image was obtained. The details of the images are given in Table 1.

2.3. APEX

The S 1 PDR was mapped in CO(6–5) and in ¹³CO(6–5) using the SEPIA-660 receiver on the 12 m Atacama Pathfinder EXperiment (APEX)³ telescope, located at Llano de Chajnantor in the Atacama high desert of Chile (Güsten et al. 2006). The observations were part of the programme m-0102.f-9524c-2018. SEPIA-660 is a SIS dual-polarization 2SB receiver with

³ APEX, the Atacama Pathfinder Experiment is a collaboration between the Max-Planck-Institut für Radioastronomie, Onsala Space Observatory (OSO), and the European Southern Observatory (ESO).

an IF bandwidth of 4-12 GHz (Belitsky et al. 2018). The backends used are advanced Fast Fourier Transform Spectrometers (Klein et al. 2012) with a bandwidth of 2×4 GHz and a native spectral resolution of 61 kHz. The rest frequencies for CO(6–5) and $^{13}\text{CO}(6-5)$ are 691.473076 GHz and 661.0672766 GHz, respectively. The HPBWs at CO(6–5) and $^{13}\text{CO}(6-5)$ are $9''.0$ and $9''.4$, respectively. The main beam efficiency η_{mb} , is = 0.53, as measured from observations of Jupiter (diameter $44.5''$)

The $^{12}\text{CO}(6-5)$ map was observed on April 19, 2019 in on-the-fly total power mode with an off position at $0'', +300''$ relative to S 1 (RA $16^h26^m34.17^s$, Dec $-24^\circ23'28.3''$). The weather conditions were good (PWV 0.66 mm) with a zenith optical depth of ~ 0.75 resulting in SSB system temperatures of ~ 1000 K. The map size was $235'' \times 200''$, centered at $(-17''5, 0)$. The field was scanned in both RA and Dec with a spacing of $4''.5$ (half the beam size) and oversampled to $3''$ in scanning direction, resulting in a uniformly sampled map with high fidelity. Unfortunately, the off position was not clean and we did a single point long integration toward a far off at $0'', +1080''$, which was used to correct the map in the post processing stage.

On April 27, 2019 we observed a smaller map in $^{13}\text{CO}(6-5)$ of the SW part of the PDR, also in OTF TP mode. The map was centered at $(-75'', 0)$ and the map size was $60 \times 120''$, with the same sampling strategy as above. The weather conditions were good (PWV 0.53 mm) with a zenith optical depth of 0.67. The SSB system temperature was ~ 800 K.

The spectra were reduced in CLASS and calibrated in T_{mb} . We removed a first order baseline and resampled the spectra to 0.5 km/s velocity resolution. The final data cubes (pixel size $9''$) after gridding have an rms main beam temperature noise per pixel of ~ 0.33 K and 0.24 K for CO(6–5) and $^{13}\text{CO}(6-5)$, respectively.

2.4. Auxiliary data

For comparison with our observations, we have used maps of the $J=3-2$ transition of CO, ^{13}CO and C^{18}O (White et al. 2015) and $J=4-3$ transition of HCO^+ , all observed with JCMT using the HARP receiver with a beamsize of $14''$. The CO (and isotopologues) spectra were observed as part of the Gould Belt Survey and the $\text{HCO}^+(4-3)$ data set, corresponding to the proposal M11AU13, was downloaded directly from the JCMT archive at the Canadian Astronomical Data Centre (CADC). Both these datasets have also been presented and compared with the previous [C II] observations of the S 1 PDR by Mookerjea et al. (2018). The emission maps of S(2) and S(3) pure rotational transitions of H_2 observed with ISOCAM-CVF by Larsson & Liseau (2017) were also used for comparison.

3. Results

3.1. Properties of the ionized gas around S 1

The radio continuum emission from ionized plasma at 610 and 1420 MHz are shown in Fig. 1. The emission at 610 MHz shows a bright core surrounded by low brightness diffuse emission. The emission is extended up to $25''$ which corresponds to 0.02 pc at a distance of 137 pc. The emission at 1420 MHz extends up to $50''$. A central bright peak is observed surrounded by low surface brightness halo emission. Both 610 and 1420 MHz images reveal an elongation in the North west-South east direction, which is more prominent in the 1420 MHz image. Such elongated structures in radio emission are often indicative of ionized jets from massive YSOs (e.g., Purser et al. 2016). The total flux densities

at these frequencies are obtained using a two component Gaussian fit to the emission. The flux density of the central unresolved source is 5.6 ± 0.2 mJy and that of diffuse halo is 41.6 ± 3.0 mJy at 1420 MHz. The flux density of the central source at 610 MHz is 6.8 ± 2.0 mJy and that of diffuse emission is 47.6 ± 2.1 mJy.

Assuming that the diffuse emission at 1420 MHz is optically thin, we have estimated the Lyman continuum photon rate and the spectral type of the star responsible for ionized emission. The Lyman continuum photon flux at 1420 MHz towards S 1 is estimated using the equation (Schmiedeke et al. 2016)

$$\left[\frac{N_{\text{Ly}}}{\text{s}^{-1}} \right] = 4.771 \times 10^{42} \left[\frac{S_\nu}{\text{Jy}} \right] \left[\frac{\nu}{\text{GHz}} \right]^{0.1} \left[\frac{T_e}{\text{K}} \right]^{-0.45} \left[\frac{d}{\text{pc}} \right]^2 \quad (1)$$

where S_ν is the flux density at frequency ν which is 41.59 mJy at 1420 MHz, T_e is the electron temperature which is found to be 8200 K based on electron temperature gradient across the Galactocentric distance (Quireza et al. 2006) and d is the distance to the source which is 137 pc (Mookerjea et al. 2018). Using the above expression, the Lyman continuum photon rate is found to be $6.7 \times 10^{43} \text{ s}^{-1}$. The estimated uncertainty in the electron temperature derived using the formulation by (Quireza et al. 2006) is ≈ 100 K. Thus, no additional uncertainty in the estimated N_{LyC} is introduced due to this. If a single main sequence star is responsible for the ionization, then the spectral type of the ZAMS star is earlier than B3V (Thompson 1984). For a B3V star with $T_{\text{eff}} = 18700$ K and $R = 4.15 R_\odot$, Kurucz model (Castelli & Kurucz 2003) gives $N_{\text{LyC}} = 5.3 \times 10^{43} \text{ s}^{-1}$ and for a B2V star with $T_{\text{eff}} = 22000$ K and $R = 5.19 R_\odot$, we get $N_{\text{LyC}} = 8.2 \times 10^{44} \text{ s}^{-1}$. Thus taking the uncertainties of the derived N_{LyC} into account, we conclude that the star S 1 is most likely B2.5V or B3V, which is not inconsistent with the SED fitting by Mookerjea et al. (2018). Although they concluded a B4V type for the star, they noted that a B3V would fit equally well if a slightly larger extinction of 13.3 mag was adopted instead of 12.7 mag.

From the VLA high frequency mapping of ρ Oph at 5 and 15 GHz, André et al. (1988) showed that the radio emission towards this region comes from a non-thermal unresolved source surrounded by a thermal extended halo. It is now known that S 1 is a close binary (Ortiz-León et al. 2017) with the secondary being responsible for the non-thermal emission. The flux density of the central source at 1420 MHz within the uncertainties is consistent with the flux measurements of André et al. (1988) and Stine et al. (1988). Using the flux densities of 6.8 and 5.6 mJy at 610 and 1420 MHz respectively, we derive a spectral index of -0.2 ± 0.3 , where the uncertainty in the derived index is contributed primarily by the uncertainty of the 610 MHz flux.

3.2. The Morphology of the S 1 PDR cavity

IRAC and MIPS images (Padgett et al. 2008; Gutermuth et al. 2009) show that S 1 illuminates a large elongated spheroidal or egg shaped cavity with the major axis at a position angle of 54° and a length of $\sim 10'.5$ and a minor axis of $\sim 5'$. There is very strong PDR emission toward south-west (SW) where it is blocked from expanding by the surrounding dense molecular cloud. Toward the north-east (NE), where the PDR shell emerges out of the cloud, the emission is rather faint and barely visible. S 1 is $\sim 80''$ from the SW tip of the PDR shell⁴. We have used

⁴ In the following we refer to NE to SW as being the direction of the major axis of the PDR shell and north-west (NW) to south-east (SE) being perpendicular to it.

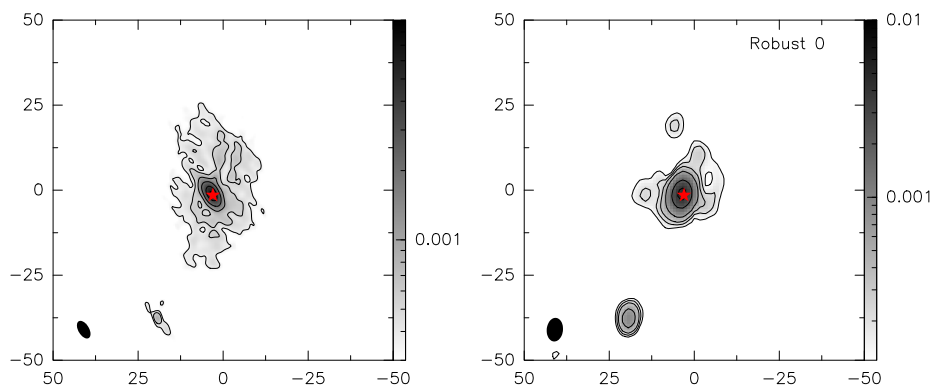


Fig. 1. Radio continuum images of the region around S 1 in ρ Oph. (Left) At 1420 MHz with contour at 0.36, 0.52, 1.0, 2.0, 4.0, 6.0 mJy/beam. (Right) At 610 MHz with contour at 0.12, 0.3, 0.6, 2.0, 4.0 and 6.0 mJy/beam. The beamsizes are shown in the bottom left corner of each panel. Asterisk marks the location of the embedded star S 1. The positional offsets (in arcseconds) are relative to the center $\alpha=16^h26^m34^s.175$, $\delta=-24^\circ 23' 28''.3$ (J2000).

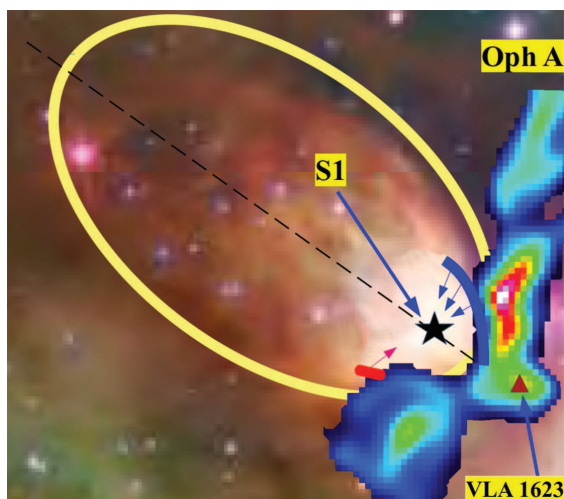


Fig. 2. Composite color image of the S 1 PDR derived using the 3.6, 4.5 and 8 μ m Spitzer observations (Padgett et al. 2008). Also shown is a cartoon of the morphology of the PDR that is derived in this paper on the basis of spatial and velocity dependence of emissions in multiple tracers. The red and blue surfaces show respectively the red- and blue-shifted fronts of the PDR. The color map corresponds to N_2H^+ emission (Larsson & Liseau 2017) from the molecular cloud to the west. The yellow line demarcates the boundary of the PDR as identified from our [C II] observations and the 8 μ m emission.

a combination of spatial and velocity information in the form of line integrated emission, velocity-channel maps as well as position-velocity diagrams along selected directions in the maps of the observed PDR tracers to understand the basic geometry of the PDR associated with S 1 (Fig. 2). To the west the PDR borders the Rho Oph A ridge, which curves to the east south of the PDR. To the NW the molecular cloud becomes very diffuse and is not seen in CO (White et al. 2015). In the past there have been no spectral line observations of the PDR emission east of S 1 and most observations did not even fully capture the PDR emission to N of S 1, which prompted Larsson & Liseau (2017) to model the PDR shell as a gaseous sphere with a radius of $80''$.

We have mapped extended regions around S 1 in several PDR tracers: [C II], [O I] 63 and 145 μ m, CO(6-5) and $HCO^+(4-3)$. Although $HCO^+(4-3)$ is not really a PDR tracer and is mainly a dense gas tracer, it does show some excess emission from the PDR (Fig. 3). These data have been compared with pre-

vious observations of the $J=3-2$ transitions of CO, ^{13}CO and $C^{18}O$ (Mookerjea et al. 2018). The emission seen in these PDR tracers match well with the emission from neutral hydrogen (H I) and other PDR tracers such as 8 μ m PAH emission and the S(2) pure rotational transition of H_2 at 12.3 μ m (Fig. 3; see also Larsson & Liseau 2017). The visual extinction toward S 1 is ~ 13.3 mag and may even be higher over part of the nebula (Mookerjea et al. 2018). Additionally, the emission from all observed PDR tracers with the exception of [O I] 145 μ m, which is optically thin, are heavily self absorbed. The [C II] F=2-1 line is also optically thin, but relatively faint and only securely detected where the [C II] emission is strong. The [O I] 63 μ m line is so strongly self absorbed, that no emission is seen in the v_{LSR} range 3-4.5 $km s^{-1}$ (Fig. 4). It is therefore unusable as a tracer of the morphology of PDR cavity. There is a strong CO(6-5) emission from the Rho Oph A ridge. However, near the SW tip of the PDR cavity the emission from the PDR starts to dominate. The CO(6-5) and [O I] 145 μ m maps also capture the dense molecular PDR to the north-east of S 1.

The channel maps of [C II] and [O I] 145 μ m (Fig. 4) show that the PDR emission is strongly red-shifted on the south-eastern side of the nebula while the emission is primarily blue-shifted on the north-western side. The H I emission is also strongly red-shifted on the south-eastern side. This implies that gas is moving away from the observer on the south-eastern side, while it is streaming toward the observer on the north-western side, although blue-shifted emission is also detected to the SE. At the SW tip of the PDR one can see both blue- and red-shifted gas. The blue-shifted emission dominates to the NW, and red-shifted emission to the SE. The same is true for the rest of the PDR nebula. This streaming gas must be due to photo evaporating gas, which is commonly seen in PDRs. On the SE side of the cavity and toward SW, the PDR emission is generally more red-shifted than the emission from the surrounding cloud. Figure 5 shows that the CO(6-5) emission traces the NW PDR boundary extremely well at velocities from 1.5-3 $km s^{-1}$ and the red-shifted filament south of S 1. The CO(6-5) emission is strongly self-absorbed in the PDR in the velocity range 3-4 $km s^{-1}$, similar to [O I] 63 μ m, though not as extreme. The emission from the filament detected in CO(6-5) is by no means smooth. It shows two clumps of emission in the velocity channels from 4.5 and 5.5 $km s^{-1}$. The CO(6-5) emission is quite faint to the East of S 1, where the [O I] 145 and [C II] emission is still quite strong. One can also see faint CO(6-5) emission NE of S 1, which may be unrelated to the PDR. The velocities of emission of the H I 21 cm

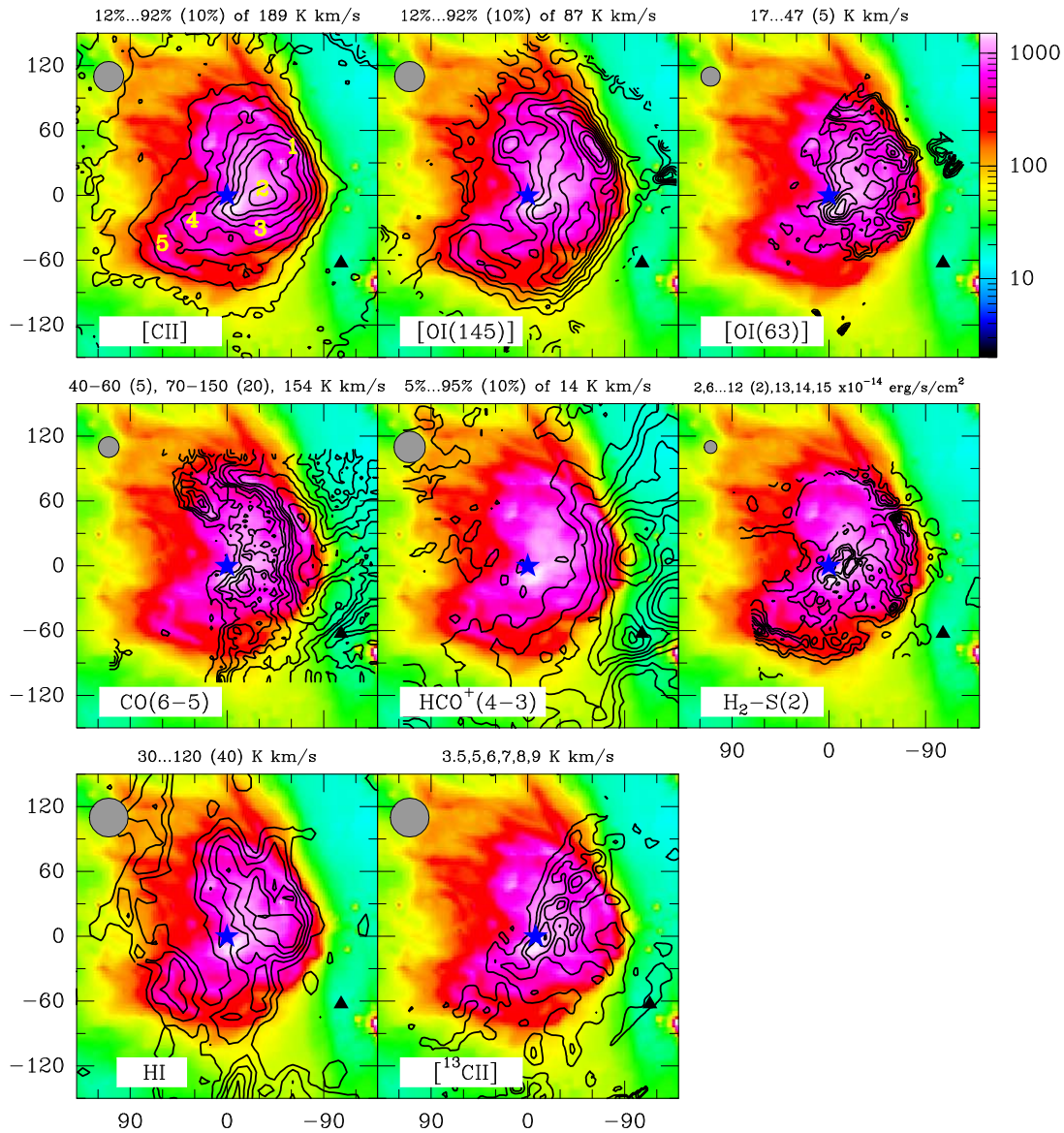


Fig. 3. Comparison of $8\ \mu\text{m}$ continuum image observed with IRAC/Spitzer (color) with contours of integrated intensity images of tracers (marked) overlaid on the $8\ \mu\text{m}$ continuum image observed with IRAC/Spitzer. The color scale is shown in the wedge to the right of the top row, with numbers in units of MJy/sr. For each of the tracers shown as contours, levels are shown on the top of the panel and beams are shown at the top left corner of each panel. The range of velocities over which integrations are done are as follows: [C II] -0.5 to $7.5\ \text{km s}^{-1}$, [O I] $145\ \mu\text{m}$ 1 to $5.5\ \text{km s}^{-1}$, [O I] $63\ \mu\text{m}$ 0.5 to $6.5\ \text{km s}^{-1}$, H I -0.5 to $5\ \text{km s}^{-1}$, CO(6–5) 0 to $10\ \text{km s}^{-1}$, HCO⁺(4–3) 0 to $10\ \text{km s}^{-1}$ and [¹³C II] F=2–1 1 to $5\ \text{km s}^{-1}$. The positional offsets are relative to the center $\alpha=16^{\text{h}}26^{\text{m}}34^{\text{s}}.175$, $\delta=-24^{\circ}23'28''.3$ (J2000). The asterisk and the triangle, mark the positions of S 1 and VLA 1623, respectively. The numbers in the top left panel mark selected positions which are studied in detail. The offsets for the positions are 1(-61,45), 2(-33,6), 3(-31,-31), 4(32,-23) and 5(60,-45).

line are in general agreement with the velocities and features traced by the PDR gas and not so much with low- J CO emission. The H I emission is strongly affected by self absorption between 3 – $6\ \text{km s}^{-1}$ and shows the east-west extended filament but only at larger velocities of 6.5 – $9\ \text{km s}^{-1}$ than the PDR gas possibly due to stronger self-absorption at lower velocities. Figure 6 shows three-color composites of [C II] and [O I]145 emission for different velocity ranges. This clearly shows that the emission at near-cloud velocities (coded green) is close to S 1, while the blue-shifted emission arises from the north-west and the red-shifted emission is to the south-east. The three-color plot of C⁺ additionally prominently shows a strong red-shifted filament just SE of S 1.

In order get a more detailed view of the S 1 PDR cavity, we created position velocity diagrams (Figs 7–10) of several PDR

tracers both along cuts parallel and perpendicular to the major axis of the cavity as shown in Fig. 6. In the following, we refer to these position-velocity diagrams as pv-cuts. The [C II] map is more extended than the other maps and in [C II] one can still see faint PDR emission $120''$ to the NE of S 1 (Fig. 7). There will be [C II] emission even further to the East, although it is likely to be faint. However, since the gas densities and FUV radiation field is low, it is possible that only the rim outlining the PDR shell can be detected. The position-velocity diagrams show that the SW tip of the PDR is somewhat red-shifted suggesting that the PDR is tilted away from us in the SW and coming toward us in the NE. The perpendicular pv-cuts across the PDR cavity show that the cavity is less extended to the SE ($\sim 80''$) than to the NW ($\sim 100''$), suggesting that the surrounding molecular cloud must be much denser on the SE side than on

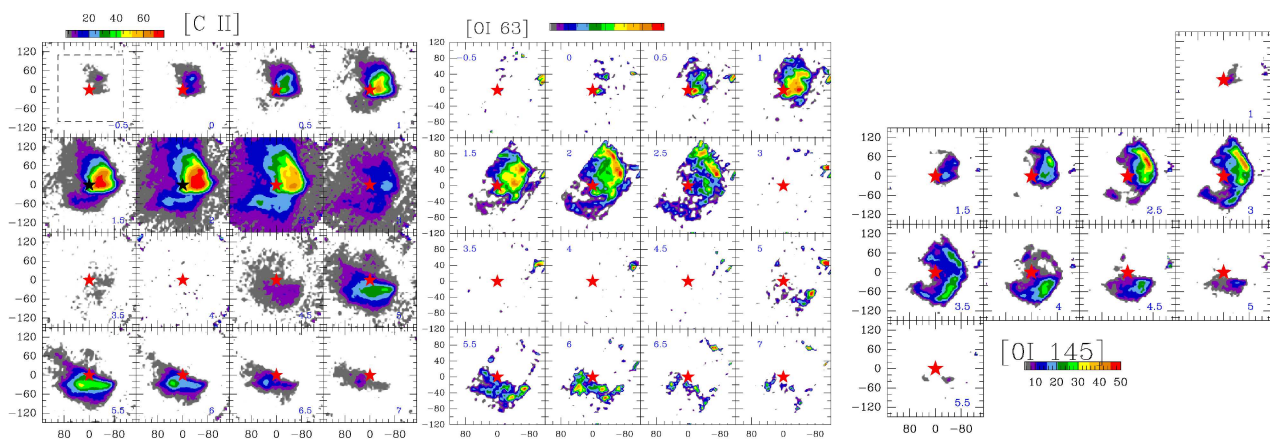


Fig. 4. Channel maps of [C II] (left), [O I] 63 μm (middle) and [O I] 145 μm (right). The color scale for each map is shown next to the map. Velocities corresponding to the channel are marked in each panel. The red star sign marks the position of S 1. The positional offsets (in arcseconds) are relative to the center $\alpha=16^{\text{h}}26^{\text{m}}34^{\text{s}}.175$, $\delta=-24^{\circ}23'28''.3$ (J2000). The area mapped in CO(6–5) is shown with dashed boundaries on the top-left panel of the [C II] channel map.

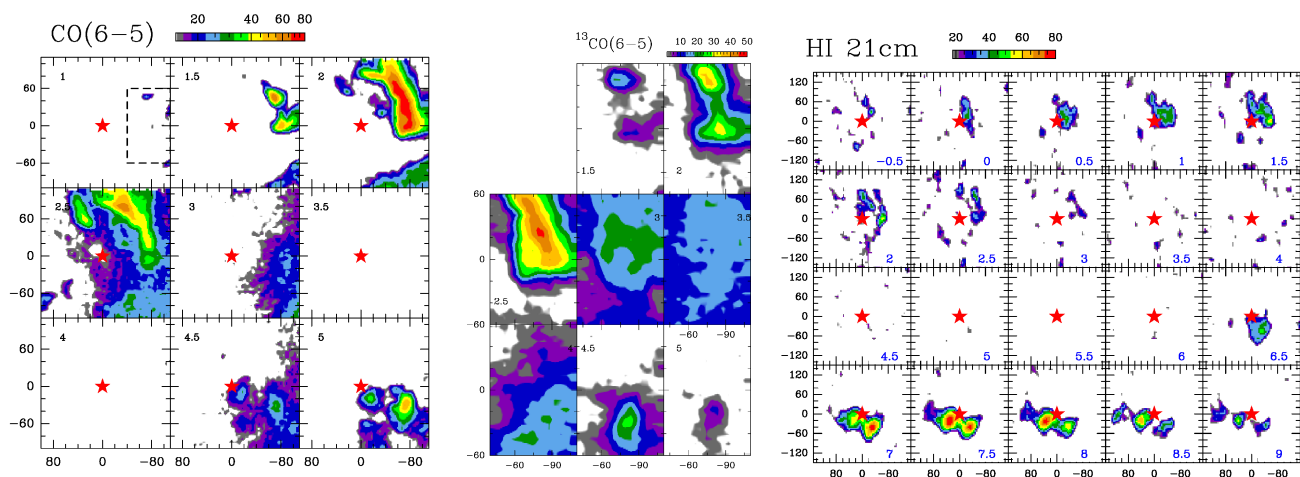


Fig. 5. Same as in Fig. 4 but for channel maps of CO(6–5) (left), ^{13}CO (6–5) (middle) and H I (right) emission. The area mapped in CO(6–5) is smaller than the maps in Fig. 4. The area mapped in ^{13}CO (6–5) is marked with dashed boundaries in the top left panel of the CO(6–5) channel map.

the NW side, which slows down the expansion of PDR cavity to the SE compared to the NW side. The perpendicular pv-cuts also show strong blue-shifted emission to the NW with more red than blue-shifted emission to the SE. The flip from red-shifted to blue-shifted emission occurs roughly at the symmetry axis of the PDR cavity. The HCO⁺ emission, which is dominated by the surrounding cloud, also shows the same velocity gradient across the PDR cavity. These pv-cuts suggest that on the SE side of the cavity the surrounding cloud must be very dense on the front side, i.e. the side facing us, while on the NW side the cloud is denser on the back side. This forces the photo evaporation flow from the PDR to be mostly red-shifted in the SE and blue-shifted in the NW. We have tried to visualize this in the cross-sectional view of the PDR SW of S 1 (Fig. 2), which is a very simplified picture, because the PDR layer is by no means smooth. There may be ridges and valleys and there can also be dense clumps of gas inside the PDR, like what appeared to be the case for NGC2023 (Sandell et al. 2015). There is a strong red-shifted filament just

SE of S 1, which stands out prominently in the [O I] 63 μm channel maps at velocities from 5 – 6.5 km s^{-1} (Fig. 4). This filament is also seen in the [O I] 145 μm , [C II], H I and CO(6–5) channel maps (Fig. 4 and 5).

3.3. Analysis of Spectral Profiles

The [C II], CO(6–5), H I spectra throughout the observed map show self-absorption, along with red- and blue-shifted line wings. The [C II] lines are the broadest among the PDR and molecular tracers. The [O I] 145 μm spectra typically show a single peak centered on the absorption in the [C II] spectra as well as an extended blue wing at a few positions. The [O I] 63 μm on the other hand is completely absorbed between 3 – 4.5 km s^{-1} . The spectra of ^{13}CO (6–5) show absorption dips at positions close to the CO(6–5) peak but is single-peaked at positions to the southwest of the map as well as in the region immediately to the west of the S 1. This suggests that the foreground material is optically

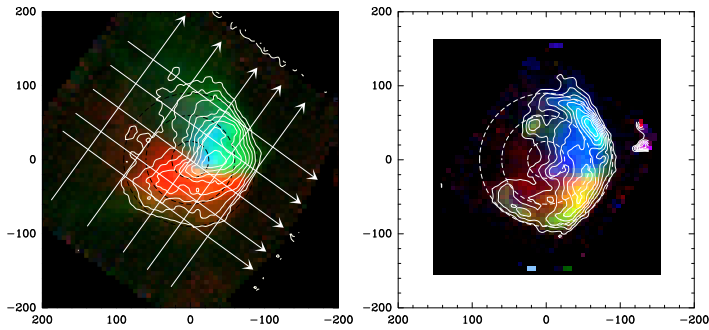


Fig. 6. Left: Three-color map of [C II] emission in velocity interval $v_{\text{LSR}} = -0.5$ – 1 km s $^{-1}$, 1.5 – 3 km s $^{-1}$ and 4.5 – 7 km s $^{-1}$ shown as blue, green and red channels respectively. The contours show the [C II] emission in the velocity interval -0.5 – 7 km s $^{-1}$. The orthogonal sets of lines show the cuts along which position-velocity diagrams are derived. Right: Three-color map of [O I] 145 μ m emission in the velocity intervals $v_{\text{LSR}} = 1$ – 2.5 km s $^{-1}$, 3 – 4 km s $^{-1}$ and 4 – 5.5 km s $^{-1}$ as blue, green and red channels respectively. The contours show the [O I] 145 μ m emission in the velocity interval 1 – 5.5 km s $^{-1}$.

thin in [O I] 145 μ m throughout the entire map, while $^{13}\text{CO}(6-5)$ is still moderately optically thick at a few positions. Figure 11 shows the spectra at the location of S 1 and five additionally selected positions (shown in Fig. 3) within the mapped region, which sample a variety of [C II] lineshapes that are representative of the entire map.

Our observations are deep enough to detect the $F = 2-1$ transitions of [$^{13}\text{C II}$] at 90 positions in the entire region. Closer inspection of the [C II] spectra at five out of the six selected positions also reveal clear detection of the $F = 2-1$ transition of [$^{13}\text{C II}$]. Unlike the [C II] profiles which show a strong absorption dip, the [$^{13}\text{C II}$] spectra peak exactly at the location of the [C II] dip (Fig. 12). Similar trends are also visible when the [O I] 63 and 145 μ m spectra are compared at these five positions (Fig. 13).

We start with trying to understand the role of the foreground material in shaping the [C II] and [O I] 63 μ m spectral profiles characterized by deep self absorption. We model the observed [C II] and [O I] 63 μ m spectra considering two layers, a background one (the main PDR) that emits and a foreground cloud that absorbs. We take an empirical approach and assume that the [$^{13}\text{C II}$] and [O I] 145 μ m spectra which are optically thin, represent (except for a *scaling factor*) the [C II] and the [O I] 63 μ m spectra respectively, that the PDR would emit in the absence of the foreground absorbing gas. The scaling factor used for the [$^{13}\text{C II}$] spectrum is $^{12}\text{C}/^{13}\text{C}=70$ (after correcting for the detection of only the strongest of the hyperfine structure line of [$^{13}\text{C II}$] which accounts for 0.625 of total [$^{13}\text{C II}$] intensity). The ratio of the [O I]63/[O I]145 intensities in the background emitting gas depends strongly on the physical conditions, here we use a scaling factor of 2 for the [O I] 145 μ m spectrum which corresponds to $F_{63\mu\text{m}}/F_{145\mu\text{m}}$ of 24, a value that is representative for warm, medium dense PDR conditions (Goldsmith 2019, e.g. Fig. 5). Thus, we consider that at each position the [C II] ([O I] 63 μ m) spectrum is given by the scaled [$^{13}\text{C II}$] ([O I] 145 μ m) spectrum and the foreground gas is a pure absorbing screen with a constant velocity, width and optical depth. In this approach we assume that the effect of the foreground material on the background emission is to attenuate the latter by the factor $\exp(-\tau_0 \exp[-4 \ln 2 (v - v_0)^2 / \Delta v^2])$. Here τ_0 , v_0 and Δv de-

note the peak optical depth, the velocity at which the foreground cloud has a value of τ_0 , and the FWHM of the foreground absorption profile. In order to generate the [$^{13}\text{C II}$] spectra with higher fidelity we have co-added the [$^{13}\text{C II}$] and all other spectra over $20''$ with centers at the selected offsets. Additionally, to improve the quality of the template spectra generated from [$^{13}\text{C II}$], and [O I] 145 μ m, we do not use the observed spectra to simulate the emission, but instead we use the Gaussian profiles generated from fits to the observed spectra. Figures 12 and 13 also show the results of such two-slab modeling at five selected positions in the observed region.

Table 2. The peak optical depth, the corresponding velocity and the FWHM of the foreground absorbing gas derived from modeling the [C II] and [O I]63 μ m spectra with a two-slab model. The $T_{\text{kin}}^{\text{min}}$ presented is an estimate of the lower limit of kinetic temperature of the [C II] emitting gas. It corresponds to the peak of the fitted background [C II] spectrum, assumed to have an optical thickness of unity.

Position	Species	Ratio	τ_0	v_{LSR} km s $^{-1}$	Δv km s $^{-1}$	N_{abs} cm $^{-2}$	T_{kin} K
(-61,45)	[C II]	70	4.7	3.5	1.4	$9.9 \cdot 10^{17}$	157
	[O I]63	2	6.8	4.0	2.2	$3.0 \cdot 10^{18}$	
(-33, 6)	[C II]	70	3.5	4.4	3.4	$1.8 \cdot 10^{18}$	121
	[O I]63	2	7.9	3.7	1.9	$3.0 \cdot 10^{18}$	
(-31,-31)	[C II]	70	4.8	3.9	1.5	$1.1 \cdot 10^{18}$	130
	[O I]63	2	8.5	3.8	1.7	$2.9 \cdot 10^{18}$	
(32,-23)	[C II]	70	3.5	3.9	2.2	$1.2 \cdot 10^{18}$	97
	[O I]63	2	4.1	3.8	1.9	$1.6 \cdot 10^{18}$	
(60,-45)	[C II]	70	4.6	3.9	1.4	$9.7 \cdot 10^{17}$	79
	[O I]63	2	6.0	4.1	1.9	$2.3 \cdot 10^{18}$	

Table 2 presents the results of fitting of the two-component model to the [C II] and [O I]63 μ m spectra. The C $^+$ absorbing layer shows peak opacities (τ_0) between 3.5–4.8 at velocities (v_0) between ~ 3.5 – 4.4 km s $^{-1}$, with a width (Δv) between 1.4– 3.4 km s $^{-1}$. The O 0 absorbing layer gives rise to peak opacities for [O I]63 μ m of 4–8, at velocities between 3.7– 4.1 km s $^{-1}$ with a linewidth of 1.7– 2.2 km s $^{-1}$.

We point out that in particular the blue part of the [C II] spectrum is not fully reproduced at some of the positions, likely due to the fact that the [$^{13}\text{C II}$] lines being fainter do not trace the line wings where [C II] is optically thin. Similarly, at (32,-23) for the fit to the [O I] 63 μ m spectrum, a broader red-shifted velocity component is completely missed out and part of the blue wing is not fully reproduced by the fit based on the [O I] 145 μ m spectra. For both (-31,-31) and (-61,45) the fits lack somewhat at lower velocities. The central velocity and linewidth of the foreground absorbing component derived for fits to both [C II] and [O I] 63 μ m spectra are consistent with the two-component LTE-based modeling that was performed by Mookerjea et al. (2018). However, the fit presented here is better constrained because of the availability of [$^{13}\text{C II}$] and [O I] 145 μ m.

Table 2 presents the column densities in the lower energy level of C $^+$ and O 0 in the foreground absorbing gas estimated based on the $\int \tau dv$ values derived from the fits and using the relation:

$$N_l = \frac{g_l}{g_u} \frac{8\pi}{\lambda^3 A_{ul}} \int \tau_{ul} dv \quad (2)$$

where, g_l and g_u denote the statistical weights of the lower and upper energy levels, A_{ul} denotes the Einstein's A-coefficient for spontaneous emission and λ denotes the wavelength of the transition.

We obtain $N(\text{O})$ of the absorbing gas to be between $(2.3$ – $3.0) \cdot 10^{18}$ cm $^{-2}$. For these column densities, based on non-LTE

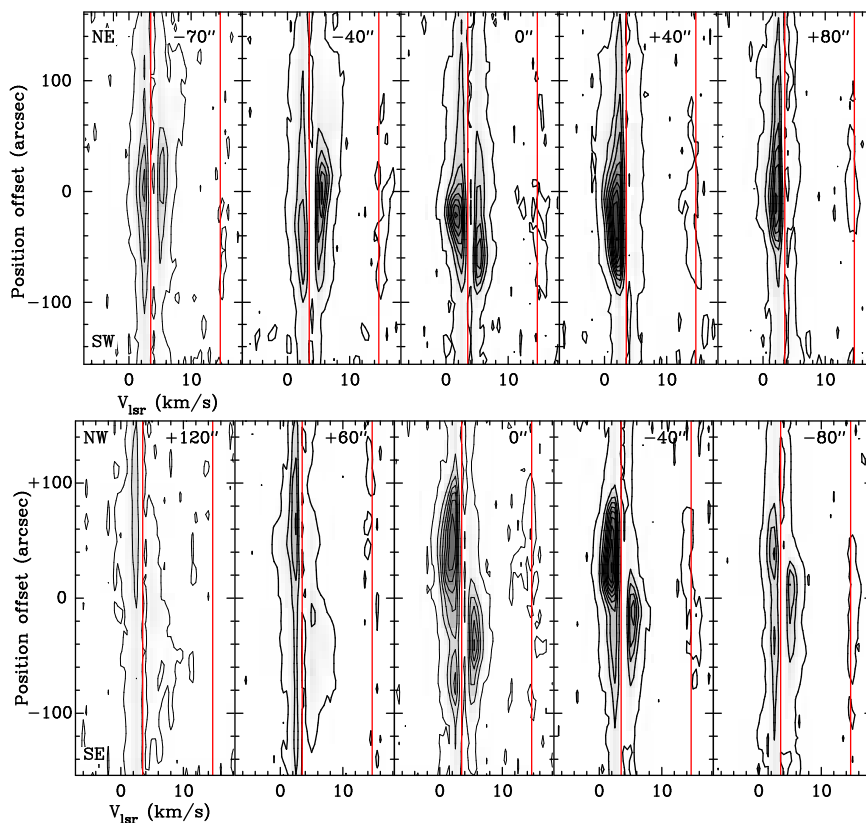


Fig. 7. Position-velocity diagrams of [C II] emission along the parallel (top) and perpendicular (bottom) cuts shown in Fig. 6. The angular resolution is $18''$. The two red vertical lines mark the $v_{lsr} = +3.5 \text{ km s}^{-1}$ for [C II] and the $^{13}\text{C II}$ $F=2-1$ hyperfine line, which is offset by $+11.2 \text{ km s}^{-1}$ in the rest frame of [C II], or $+14.7 \text{ km s}^{-1}$. The contour levels are plotted with linear step size and enhanced with gray scale from 1 K to 1.25 times peak temperature. For the parallel cuts 10 contours from 1–73 K with the peak temperature at 73.1 K are shown. The contour levels for the perpendicular pv-plots are: 10 linear contours from 1–76 K and gray scale from 1–96 K. Offsets are relative to S 1, which is at $0''$. The parallel cuts go from NE to SW starting from the South. The perpendicular cuts go from NW to SE and start East of S 1.

calculations using RADEX (van der Tak et al. 2007), over a large range of temperatures (20–300 K) and volume densities (10^4 – 10^7 cm^{-3}) the [O I] $145 \mu\text{m}$ line is optically thin. This is also consistent with our observations. Since the T_A ratio for the two [O I] lines depends on the physical conditions, there is significant uncertainty in the derived values of the peak optical depth, although the fitted central velocity and linewidth are fairly robust against the assumed scale factor. Further, the estimate of $N(\text{O}^0)$ assumes that all O atoms in the absorbing layer are in the ground $^3\text{P}_2$ level, which is reasonable since [O I] $145 \mu\text{m}$ is not seen in absorption. We estimate the column density of C^+ in the absorbing gas to be between $(1-2) 10^{18} \text{ cm}^{-2}$. We note, that the estimate of $N(\text{C}^+)$ assumes that more than 95% of the C^+ are in the ground state. For excitation temperatures of foreground gas higher than 25 K, the derived $N(\text{C}^+)$ is a lower limit. Thus the $N(\text{O}^0)/N(\text{C}^+)$ ratio in the foreground absorbing layer is between 2–3.

This toy model confirms that both the [C II] and [O I] $63 \mu\text{m}$ spectra are strongly self-absorbed by the foreground PDR gas. Additionally, based on the derived velocity at which the peak optical depth occurs for both species ($>3.2 \text{ km s}^{-1}$), we also find that the absorption occurs due to the temperature gradient in the PDR gas itself and not due to the ambient molecular gas traced by the $J=3-2$ transitions of CO and its isotopologues.

3.4. Temperature of [C II] emitting PDR gas

In our analysis of the absorption features in the [C II] profile, we have considered the background [C II] profile to be an optically thin scaled-up version of the $^{13}\text{C II}$ profile. However, based on the recent [C II] observations of most of the Galactic PDRs it is likely that the background PDR emission is likely to have an optical depth close to 1. Guevara et al. (2020) performed an elaborate fitting procedure involving multi-component LTE components to explain optically thick background [C II] spectra that are absorbed by a foreground layer of gas. Here we approximate the background [C II] spectrum, by assuming it to be a scaled up version of the $^{13}\text{C II}$ spectrum modulated by an optical depth of 1. The Planck-corrected peak of the optically thick [C II] spectrum so derived provides a lower limit of the temperature of the [C II] emitting PDR gas. Table 2 also presents the temperatures of the [C II] emitting PDR gas at the selected positions estimated using this method.

We use the integrated line intensities of the optically thin $^{13}\text{C II}$ spectra at these selected positions to estimate $N(\text{C}^+)$. We estimate the total integrated intensity of $^{13}\text{C II}$ by considering that the observed $F=2-1$ transition accounts for 62.5% of the

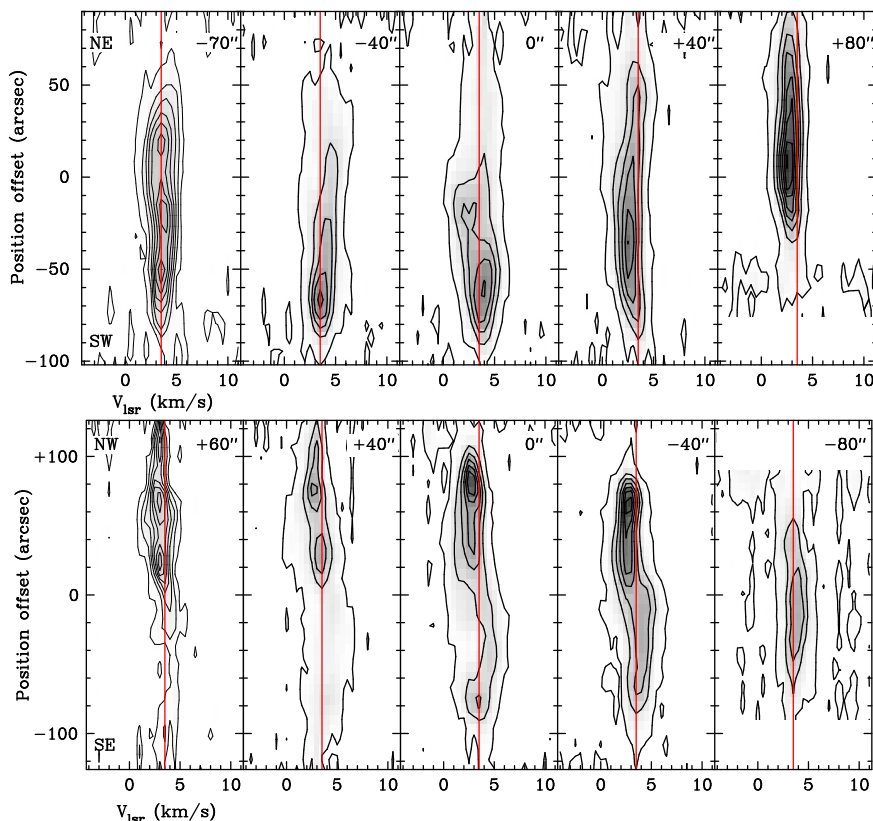


Fig. 8. Position-velocity diagrams of [O I] $145\ \mu\text{m}$ emission along the same parallel (top) and perpendicular (bottom) cuts as [C II] in Fig. 7. The angular resolution is the same as for [C II], i.e., $18''$. Eight linear contours going from 1.25–42 K are shown, while the gray scale is between 1.25–52.9 K.

total intensity (Table 3). The column density of $^{13}\text{C}^+$ is estimated following Eq (26) from Goldsmith et al. (2012):

$$N(^{13}\text{C}^+) = \frac{8\pi k_B v_{ul}^2}{A_{ul} h c^3} \left[1 + 0.5 e^{91.25/T_{\text{kin}}} \left(1 + \frac{A_{ul}}{C_{ul}} \right) \right] \int T_{\text{mb}} dv \quad (3)$$

where, $v_{ul} = 1900.4661\ \text{GHz}$, $A_{ul} = 2.3 \times 10^{-6}\ \text{s}^{-1}$, T_{kin} is the gas kinetic temperature, the collision rate is $C_{ul} = R_{ul}n$ with R_{ul} being the collision rate coefficient with H_2 or H^0 which depends on T_{kin} and n is the volume density of H. For $n_{\text{H}} > 10^4\ \text{cm}^{-3}$, $C_{ul} \gg A_{ul}$ so that the last term in Eq. 3 can be neglected.

We assume a $^{12}\text{C}/^{13}\text{C}$ ratio of 70, based on the Galactocentric distance of the S 1 PDR (Wilson & Rood 1994), using the observed integrated [^{13}C II] intensities and the estimated T_{kin} (Table 2), we estimate $N(\text{C}^+)$ at the selected positions to be between $1.3\text{--}3.8 \times 10^{18}\ \text{cm}^{-2}$ (Table 3). Comparing the total C^+ column density derived here with $N(\text{C}^+)$ estimated for the foreground absorbing gas (Table 2), we find that for all positions the column density of the colder foreground gas is approximately one-third of the $N(\text{C}^+)$ of the background PDR gas.

4. The S 1 PDR

Figure 14 shows a comparison of the observed distribution of the PDR and high density tracers with the molecular hydrogen column density, dust temperature and FUV intensity, all derived from dust continuum detected with PACS as part of the Herschel

key program on Gould Belt Survey (André et al. 2010). The column density and dust temperature maps are directly taken from the Gould Belt Survey website and we have estimated the FUV intensity from the observed far-infrared (FIR) intensity as described in Mookerjea et al. (2018). The circles drawn in Fig. 14 are centered on S 1 with radii of 45 and 75'' to guide the eye. The column density peak in the Oph A cloud is close to the position of VLA 1623. The dust temperature peaks at a position slightly offset from S 1 and closer to the [C II] peak and the embedded YSO LFAM9. The peak in the FIR continuum map is located close to S 1 and also to the south-west (Fig. A.1. in Mookerjea et al. 2018). As indicated earlier, the PDR is bound by the dense ambient cloud to the south-west and is more tenuous to the north-east. Thus, the fraction of stellar FUV radiation intercepted by the cloud is likely to be larger towards the south-west than at positions towards the east and north-east which are radially equidistant from S 1. The [C II] traces the entire PDR gas, which is also seen in the FUV map derived from the FIR continuum maps. The [O I] $145\ \mu\text{m}$ which has a higher critical density preferentially picks up the denser and warmer edge-on PDR rim to the west. The CO(6–5) traces only the PDR clumps within a very narrow strip and the $\text{HCO}^+(4\text{--}3)$ traces the higher density (and column density) molecular clouds in the Oph A ridge, which also harbors the YSO VLA 1623.

Table 3 presents results of fitting Gaussian profiles to the optically thin spectra of [^{13}C II], [O I] $145\ \mu\text{m}$, $\text{C}^{18}\text{O}(3\text{--}2)$ and $^{13}\text{CO}(6\text{--}5)$ at the positions already analyzed in Fig. 12. We find

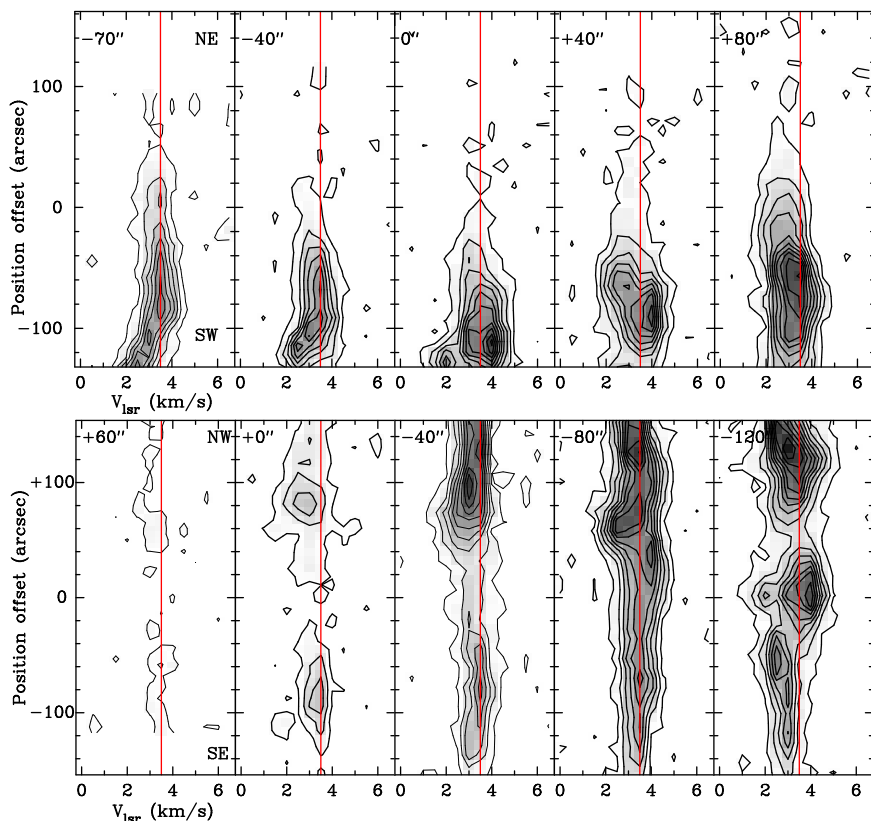


Fig. 9. Position-velocity diagrams of $\text{HCO}^+(4-3)$ emission along parallel (top) and perpendicular (bottom) cuts shown in Fig. 6 and plotted the same way as Figs. 7 & 8 using the same angular resolution as for $[\text{C II}]$. Ten linear contours from 0.3–6.9 K are shown and their peak intensity is 7.0 K. To the NE, the HCO^+ is barely detectable 60'' from S 1 confirming that the density of the surrounding cloud falls off towards the NE. The southwestern most perpendicular position velocity cut 120'' west of S 1 does not cross the PDR, but is plotted to illustrate that the emission in the Rho Oph A ridge is more blue-shifted than the emission from the S 1 PDR.

that the $[\text{C II}]$ and $[\text{O I}]145$ lines are significantly broader than the $^{13}\text{CO}(6-5)$ lines, except at the position (-61,45) which corresponds to the peak of $[\text{O I}] 145 \mu\text{m}$ as well as $^{13}\text{CO}(6-5)$. Additionally, the central velocities of the PDR tracers are red- and blue-shifted relative to the molecular cloud tracers depending on whether the positions are to the north or south of S 1 respectively. The $\text{C}^{18}\text{O}(3-2)$ primarily traces the ambient molecular cloud and hence typically peaks around 3.1 km s^{-1} .

4.1. The FUV field

The distribution and emission from the PDR is primarily a function of the FUV ($6 \text{ eV} \leq h\nu < 13.6 \text{ eV}$) radiation field and volume density of the PDR gas. The star S 1 is the primary source of FUV radiation for this PDR. Based on the observed radio continuum flux at 1420 MHz we estimate the S 1 to have a spectral type of B2.5–B3V. We thus used the Schmidt-Kaler relation for a B3V star ($T_{\text{eff}}=18,700 \text{ K}$ and a radius of $4.15 R_{\odot}$) and Kurucz model atmosphere to estimate the FUV radiation field distribution considering only projected distances and geometrical dilution. The FUV field is typically expressed in units of the Habing (1968) value for the average solar neighborhood FUV flux, $1.6 \times 10^{-3} \text{ ergs cm}^{-2} \text{ s}^{-1}$. We find that at a radial distances of 45'' and 75'' from S 1 the unattenuated FUV field from S 1 is 2.70×10^4 and $8500 G_0$, respectively. An alternative method

of estimating the strength of the FUV radiation in the region involves the use of the observed total far-infrared (FIR) intensity, assuming that the entire FUV energy is intercepted and absorbed by the grains and is reradiated in the FIR. We used the far-infrared observations of Herschel/PACS to estimate the values of FUV radiation field around S 1 (Fig. 14). We find that the observed FIR distribution is neither spherically symmetric around S 1, nor does it peak at the position of S 1. The peak in FIR emission (coinciding with the peak T_{dust}) is primarily to the north-west, where the derived FUV radiation is around $4000 G_0$ at a radius of 75''. To the east at similar radii from S 1 the estimated FUV emission is $\sim 1200 G_0$. By making a pixel to pixel comparison, we find that only for the ridge-like structure to the north-west the FUV flux predicted from the S 1 FUV radiation and from the FIR continuum agree to within a factor of 2. For regions between 40'' to 75'' from S 1 and at the ridge in the west, the two estimates differ by up to a factor of 10. The discrepancy between the FUV radiation field derived theoretically considering only geometric dilution and the field derived indirectly from the observed far-infrared radiation can be due to: (a) the emission in far-infrared continuum arising from regions, which are at much larger distances than the projected distance used here (b) FUV radiation escaping the region without being intercepted by material particularly to the east and north-east, (c) presence of very high A_V clumps, which attenuate the FUV drastically but

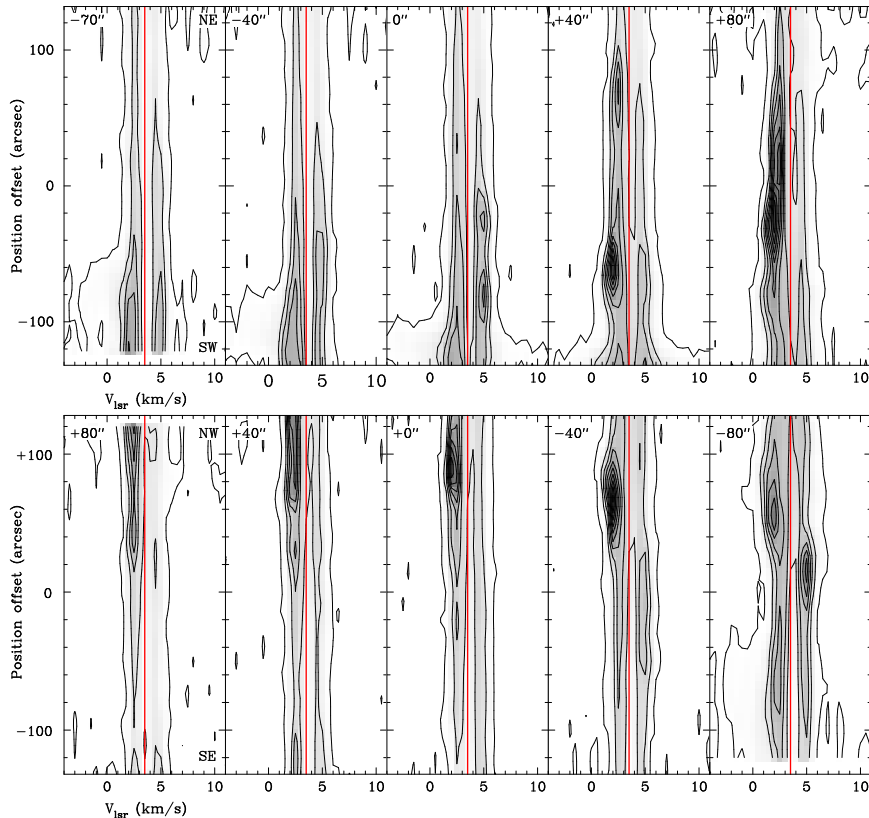


Fig. 10. Position-velocity diagrams of CO(6–5) emission along parallel (top) and perpendicular (bottom) cuts shown in Fig. 6 and plotted the same way as Figs. 7 & 8 using the same angular resolution as for [C II]. Ten linear contours from 0.8–68 K are shown and the gray scale goes from 0.8–85 K. In the parallel cuts red- and blue-shifted emission from the VLA 1623 outflow in the SW are observed. The blue-shifted outflow lobe in the SE is detected in the perpendicular cut 80'' from S 1. This bipolar outflow is unrelated to the S 1 PDR. There is no evidence for PDR emission in the perpendicular cut 80'' NE of S 1. The CO(6–5) emission is faint and most likely from the surrounding molecular cloud.

are too small to be detected in single-beam continuum observations.

As discussed in Sec 3.1, the region is bound in the west and south-west by the dense Rho Oph A ridge and possibly freely expanding to the north-east. The structures visible in the far-infrared continuum images primarily trace the column density of dust (and gas) along the lines of sight, as is shown in the H₂ column density maps generated from the same PACS maps (Fig. 14). The lower levels of FIR continuum emission closer to S 1, as well as to the east is therefore a result of lower column densities of dust (and molecular gas) in these regions, while the higher FIR continuum emission to the north-west indicate the presence of higher column density clumps, which is also substantiated by the detection of HCO⁺(4–3) with JCMT and NH₃ with the Green Bank Telescope (Friesen et al. 2017).

4.2. Comparison of observed intensities with PDR models

We compare the observed intensities of optically thin tracers [¹³C II], [O I] 145 μ m and ¹³CO(6–5) with the predictions of plane-parallel steady-state PDR models, which self-consistently calculate the intensities as a function of the FUV flux and gas density of H nuclei n_{H} . These PDR models are from an updated version of the models by Kaufman et al. (2006) (Wolfire, private communication). We perform the analysis at the five selected po-

sitions, since these lie at different radial distances from S 1 to the east-west and north-south of S 1, thus tracing the distribution of the spectral lines arising from PDR reasonably well. The S(2) and S(3) transitions of H₂ are produced by FUV pumping, and hence the intensities are proportional to the FUV radiation. At the positions where the rotational lines of H₂ S(2) and S(3) have been detected, we have also compared their intensities with the PDR model predictions. Figure 15 shows a comparison of the observed intensities of the tracers (shown as contours) with the values predicted by the models. The lower and upper limits of the FUV intensities (shown by dashed horizontal lines in Fig. 15) are determined by the values derived from the FIR intensities and from the stellar FUV radiation field, respectively (Sec. 4.1). At most positions the observed [¹³C II] exceed the intensities predicted by the models for the entire parameter space explored, hence the corresponding contours are not visible in Fig. 15.

The critical densities (and E_u) for [¹³C II], [O I] 145 μ m and CO(6–5) are 3000 cm⁻³ (91 K), 5.8×10⁶ cm⁻³ (325 K), 2.9×10⁵ cm⁻³ (116 K), respectively. The S(2) and S(3) transitions of H₂ have critical densities (and E_u) of 2.2×10⁵ cm⁻³ (1682 K) and 9.4×10⁵ cm⁻³ (2504 K), respectively. Thus [O I]145, ¹³CO(6–5) and S(2) H₂ transitions could arise from PDR gas of similarly high densities, while [¹³C II] traces the low-density PDR. Though the H₂ lines have rather high critical densities and high upper energy levels, these are produced by FUV pumping. For

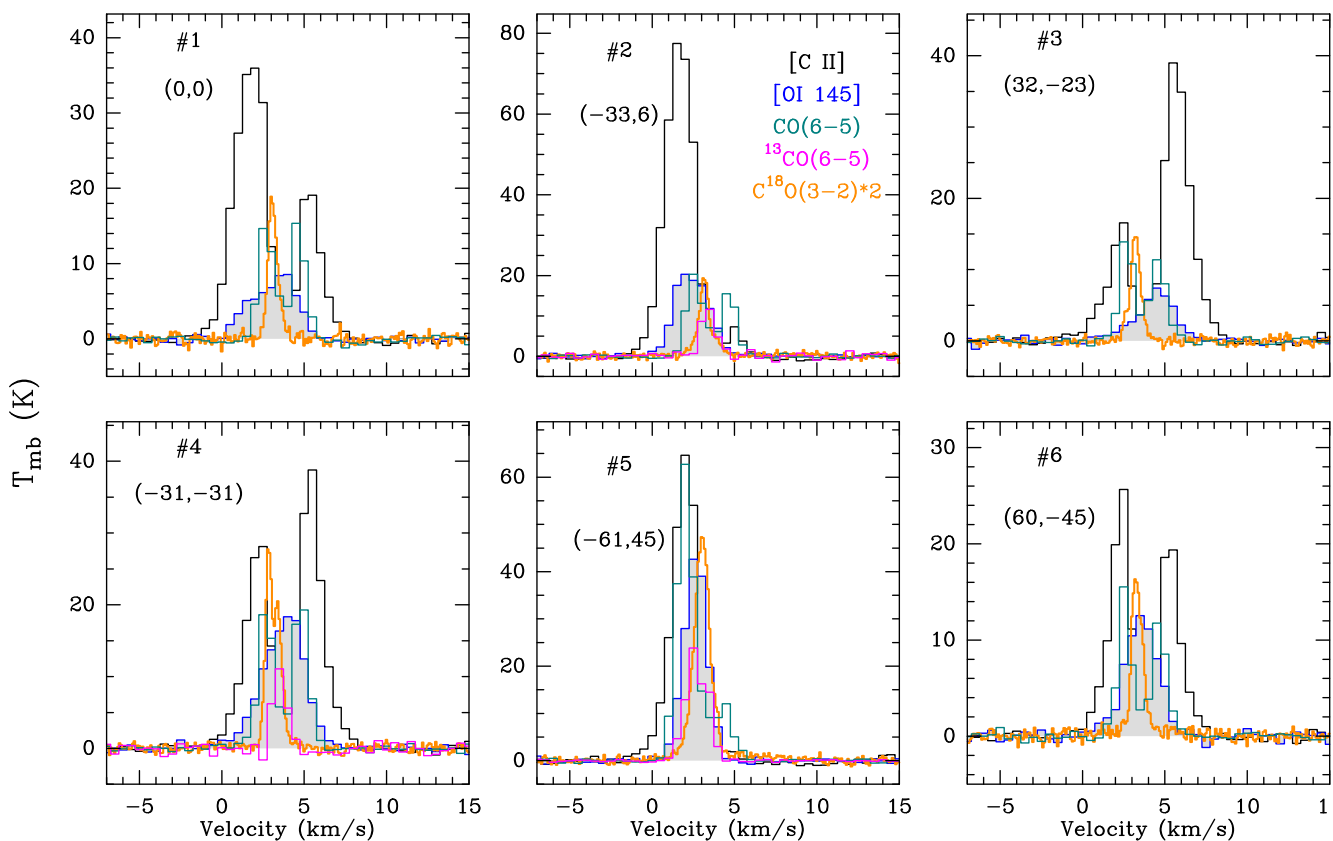


Fig. 11. Comparison of spectra of [C II], [O I], C¹⁸O(3–2), CO(6–5) and ¹³CO(6–5) transitions at the selected positions. The positions are shown in Fig. 3. The dataset corresponding to the C¹⁸O(3–2) spectra shown here were presented by Mookerjea et al. (2018). All spectra shown have been co-added across a 20'' field.

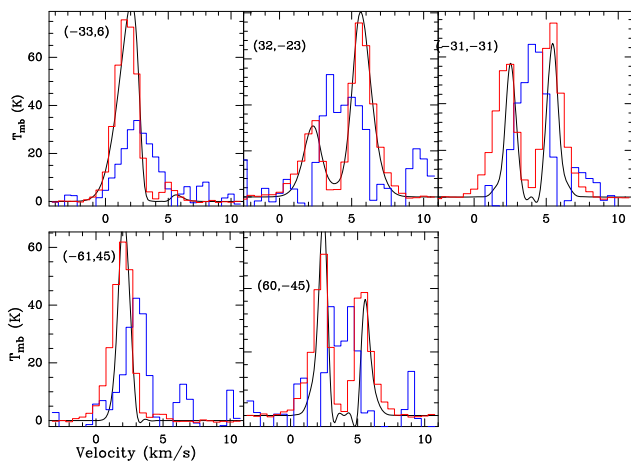


Fig. 12. Comparison of [C II] (red) and [¹³C II] (blue) spectra averaged over 20'' with centers at offsets shown in the panels. The [¹³C II] spectra have been scaled by a factor of 20 to make the spectra visible alongside [C II]. The smooth curve (black) shows the fit to [C II] spectrum obtained by attenuating the scaled [¹³C II] spectrum by the absorption due to the foreground cloud.

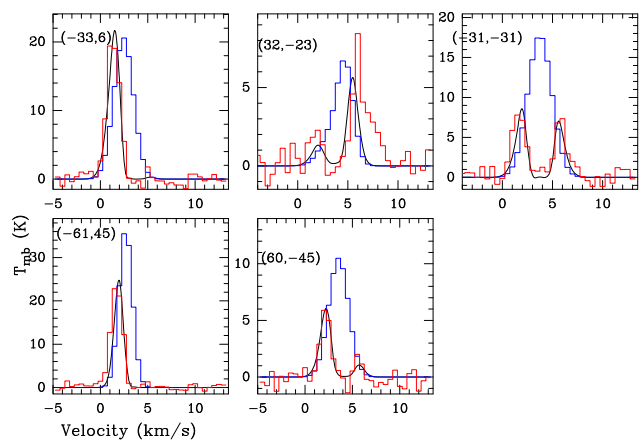


Fig. 13. Comparison of [O I] 63 (red) and [O I] 145 μ m (blue) spectra co-added over 14'' with centers at offsets shown in the panels. The smooth curve (black) shows the fit to the [O I] 63 spectrum obtained by attenuating the scaled (by a factor 2 corresponding to the typical ratio between the two [O I] lines in temperature units) [O I] 145 μ m spectrum by absorption due to foreground material.

values of $G_0/n < 10^{-2}$ the intensities of the S(2) and S(3) lines of H₂ depend on the FUV intensities while for $G_0/n > 10^{-2}$ the same intensities are indicators of the densities (Kaufman et al. 2006). At the selected positions, the FUV radiation field lies between 10^3 – $10^{4.5}$, which implies that $G_0/n = 10^{-2}$ corresponds to $n=10^5$ – $10^{6.5}$ cm⁻³. For most positions the [O I]145 and H₂ line

intensities indicate $n \sim 10^4$ cm⁻³ while ¹³CO(6–5) where detected suggest $n > 10^5$ cm⁻³. For most positions, the observed [¹³C II] intensities exceed the intensities predicted by the model corresponding to the densities indicated by the [O I]145 and the

Table 3. Results of fitting Gaussian profiles with single velocity components to observed spectra at selected positions. $N(\text{C}^+)$ is calculated assuming the lower limits of kinetic temperature, $T_{\text{kin}}^{\text{min}}$ from Table 2.

$(\Delta\alpha, \Delta\delta)$	Transition	I K km s ⁻¹	v_{LSR} km s ⁻¹	Δv km s ⁻¹	$N(\text{C}^+)$ cm ⁻²
(-61,45)	[¹³ C II]	3.99±0.38	2.97±0.1	1.74±0.2	2.8(18)
	[O I]145	70.77±0.33	2.67±0.1	1.79±0.1	
	¹³ CO(6-5)	36.63±0.22	2.71±0.1	1.65±0.1	
	C ¹⁸ O(3-2)	19.25±0.09	3.08±0.1	1.09±0.1	
	H ₂ S(2)			1.5×10 ⁻⁴	
	H ₂ S(3)			1.0×10 ⁻⁴	
(-33,6)	[¹³ C II]	5.33±0.42	2.55±0.1	3.08±0.3	3.8(18)
	[O I]145	50.77±0.47	2.45±0.1	2.55±0.1	
	¹³ CO(6-5)	12.62±0.68	3.41±0.1	1.03±0.1	
	C ¹⁸ O(3-2)	6.73±0.11	3.06±0.1	0.90±0.1	
	H ₂ S(2) ^a			1.0×10 ⁻⁴	
	H ₂ S(3) ^a			2.0×10 ⁻⁵	
(-31,-31)	[¹³ C II]	4.34±0.29	4.02±0.1	2.28±0.2	3.4(18)
	[O I]145	48.21±0.47	3.80±0.1	3.02±0.1	
	¹³ CO(6-5)	11.48±0.60	3.50±0.1	0.97±0.1	
	C ¹⁸ O(3-2)	10.83±0.10	3.10±0.1	0.90±0.1	
	H ₂ S(2) ^a			1.2×10 ⁻⁴	
	H ₂ S(3) ^a			3.5×10 ⁻⁵	
(32,-23)	[¹³ C II]	3.34±0.35	4.25±0.2	2.74±0.3	3.0(18)
	[O I]145	19.17±0.50	4.35±0.1	2.93±0.1	
	C ¹⁸ O(3-2)	4.77±0.09	3.20±0.1	1.09±0.1	
	H ₂ S(2) ^a			3.0×10 ⁻⁵	
	H ₂ S(3) ^a			1.1×10 ⁻⁵	
	[¹³ C II]	1.95±0.24	3.91±0.2	2.20±0.3	
[O I]145	24.27±0.67	3.58±0.1	2.42±0.1		
C ¹⁸ O(3-2)	6.50±0.10	3.23±0.1	0.81±0.1		
H ₂ S(2) ^a			8.8×10 ⁻⁵		
	H ₂ S(3) ^a			1.4×10 ⁻⁵	

^a H₂ data taken from Larsson & Liseau (2017) and intensities expressed in units of erg sec⁻¹ cm⁻² sr⁻¹.

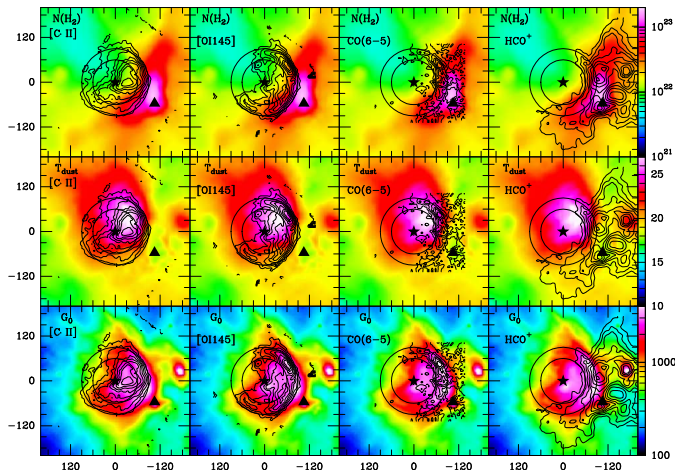


Fig. 14. Comparison of distribution of [C II], [O I] 145 μm , CO(6-5) and HCO⁺(4-3) emission vis-a-vis the column density, dust temperature and FUV intensities estimated from PACS continuum data observed as part of Herschel Gould Belt Survey. The color scales are shown to the extreme right of each row of panels. The contour levels for [C II], [O I] 145 μm and HCO⁺(4-3) are at 20–100% (in steps of 10%) of the peak values of 191, 88 and 14 K km s⁻¹ respectively. For CO(6-5) the contours are at 40–100% of the peak of 136 km s⁻¹. Circles drawn correspond to radii of 45'' and 75''.

estimated range of FUV radiation fields, by factors of 1.2–3. The largest discrepancy, a factor of 3–6, is seen at the position (-33,6). Additionally, the model predictions for the [O I]145/[¹³C II] intensity ratios indicate unrealistically high (for [¹³C II] emission) densities at all positions, that is not corroborated by the high-density tracers such as CO(6-5) and HCO⁺(4-3).

Comparison of the observed emission from the S1 PDR with models clearly shows the contributions of gas at primarily

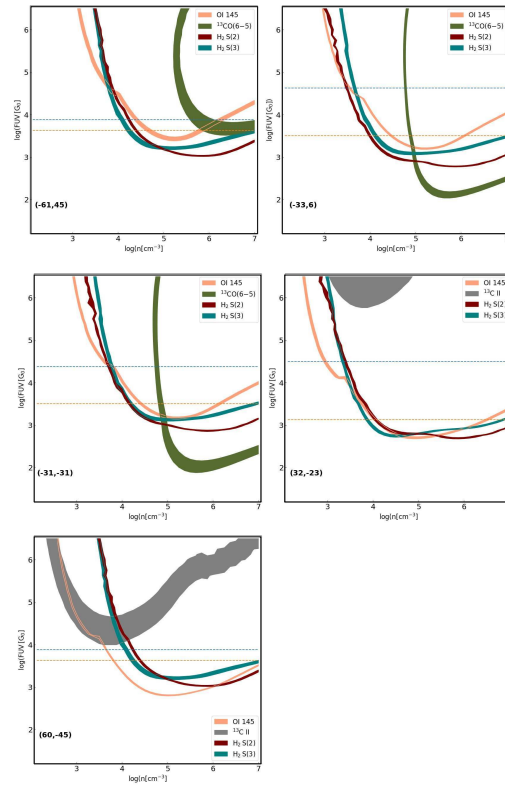


Fig. 15. Comparison of observations with prediction of line intensities as function of n_{H} and G_0 from an updated version of the Kaufman et al. (2006) PDR models (Wolfire private communication). For all positions except (32,-23) and (60,-45) the [¹³C II] intensities are beyond the values predicted by the models. The horizontal dashed lines correspond to the values of G_0 estimated from the FIR intensities (lower) and from the stellar FUV radiation scaled only by geometrical dilution due to the increase in distance from S 1.

three different density regimes, 10^5 – 10^6 cm⁻³, $10^{3.5}$ – $10^{4.5}$ cm⁻³ and $< 10^{3.5}$ cm⁻³, although the [¹³C II] emission is significantly under-produced by the models as is seen both from the [¹³C II] intensity and the [O I]145/[¹³C II] intensity ratio. The highest density regions are traced by ¹³CO(6-5) and to some extent by [O I] 145 μm . Additionally, [O I] 145 μm emission is excited in the medium density gas as well, which is also traced by the H₂ S(2) and S(3) lines. The most diffuse component is primarily traced by the [¹³C II] and for the positions (-33,6) and (-61,45) the observed intensities, estimated to be only from the diffuse component still far exceed the values predicted by the PDR models.

The lower [¹³C II] intensities and correspondingly high [O I]145/[¹³C II] ratio predicted by the face-on uniform density plane-parallel PDR models can not both be explained either by stacking layers of such PDRs along the line-of-sight or by changing the viewing angle of the model. The most plausible explanation for higher observed [¹³C II] intensities relative to [O I]145 line is in terms of the higher filling factor of the [¹³C II] emission, which typically should have significant contribution from the diffuse

gas than from the high density gas emitting mostly in [O I]145. Such discrepancies are also expected to arise from the shadowing effects of clumps as well penetrability of non-uniform density PDRs consisting of clump and inter-clump gas (Stutzki et al. 1988). Use of three-dimensional PDR models with inhomogeneity is needed, however such models also involve additional parameters which need to be pre-determined using other observational constraints. In the case of the S 1 PDR, the self-absorption of the main PDR tracers and the complex geometry of the region does not allow us to further observationally constrain the parameters for such clumpy PDR models. Qualitatively we can conclude that the fraction of [¹³C II] intensity putatively arising from diffuse PDR gas being higher towards the west of S 1 is likely to be an indicator of increased clumpiness towards the west.

5. Discussion & Conclusion

Presence of multiple emission and absorption components along the line of sight towards the PDR associated with the S 1 star in the ρ Ophiuchus molecular cloud, results in complicated spectra that are difficult to interpret. In this region, the emission arising from the PDR as well as the molecular cloud overlap, most spectra are self-absorbed and there are additional foreground filaments which criss-cross the region. The S 1 PDR is restricted by the dense Oph A molecular cloud to the west and south-west and appears to be expanding freely to the east. The PDR is tilted and somewhat warped with the front surface (facing the observer) of the south-eastern side of the cavity being very dense and on the NW side the cloud is denser on the back side. The gas distribution in the PDR is rather inhomogeneous with clumps and ridges arising due to the disruption of the dense ambient molecular cloud by the radiation from the star S 1 and also by the embedded YSOs. Analysis of the emission from the photon dominated gas suggests the presence of at least three density components consisting of high density (10^6 cm^{-3}) clumps and medium density (10^4 cm^{-3}) and diffuse (10^3 cm^{-3}) interclump medium.

Using the velocity information and the optically thin spectra of [¹³C II] and [O I] 145 μm we have shown that the absorption features in [C II] and [O I] 63 μm arise due to the foreground layers of the same PDR. The ratio of column densities of C⁺ and O⁰ in the diffuse foreground PDR layers, within the limits of uncertainties introduced particularly by the assumed value of the scaling factor for the [O I] lines is between 2–3, which is comparable to the solar [O]/[C] abundance ratio of 3.5. Spectral analysis of our data allows to qualitatively constrain the temperature of the absorbing layers. The presence of heavy foreground absorption in the [O I]63 spectra, but the complete absence of self-absorption in the [O I]145 line profiles suggests a low-excitation status of the foreground gas - low compared to the energy of the OI ³P₁ level which is 227 K above ground. On the other hand, the prominent self-absorption in the CO(6–5) line points to a somewhat elevated temperature of the absorbing gas, sufficient to populate the J=5 level (80 K above ground).

The [C II] spectra show the self-absorption dips even far to the east and the rarer isotope ¹³C⁺ has been detected at a large number of positions, suggesting an $N(\text{C}^+) \sim$ of a few times 10^{18} cm^{-2} over an extended region. The estimated $N(\text{C}^+)$ lie within the typical range of values between 10^{18} – 10^{19} cm^{-2} that is found in Galactic PDRs (Ossenkopf et al. 2013; Mookerjea et al. 2019). The H₂ column density estimated from dust continuum emission maps range between 1–2.5 10^{22} cm^{-2} at these positions. This suggests values of [C⁺/H₂] ranging between (1.5–4.8) 10^{-4} which leads to C⁺/H = (0.8–2.4) 10^{-4} . The derived value of C⁺/H

is consistent with the value C⁺/H = 1.5×10^{-4} obtained considering solar abundance with the assumption that half of the carbon is in C⁺. The uncertainties in the value of $N(\text{C}^+)$ arise due to the assumed values of T_{kin} used, which were derived from the peak of the planck-corrected [C II] spectra (Sec. 3.4) and are likely a lower limit to the temperature.

Based on the comparison of the observed intensities with the PDR models (Fig. 15) we have identified the range of densities which could explain the [O I] 145 μm intensities. We find that for the [O I] 145 μm peak, densities between 10^4 – 10^5 cm^{-3} can explain the [O I]145 intensities. Using non-LTE approximations, the observed intensities for these densities can only be explained by T_{kin} > 100 K (consistent with our derived T_{kin}^{min} of 157 K) and for $N(\text{O}^0)$ between $(1.5\text{--}3) \times 10^{19} \text{ cm}^{-2}$. Similar considerations suggest that for the positions (-33,6) and (-31,-31) the observed intensities can be explained by a T_{kin} of 100 K and $N(\text{O})$ of $(2\text{--}3) \times 10^{19} \text{ cm}^{-2}$ for $n = 10^5 \text{ cm}^{-3}$. For these two positions the lower-density-higher-G₀ solution require T_{kin} = 120 K and $N(\text{O}) = 5 \times 10^{19} \text{ cm}^{-2}$. However, we emphasize that it is likely that both the high- and low-density gas with possibly different filling factors contribute to the emission. For positions to the west of S 1, as pointed out earlier, the FUV flux derived from FIR intensities is lower than the value expected from the estimated stellar radiation since part of the radiation is not intercepted by dust. For these positions the higher FUV radiation values corresponding to the geometrically diluted stellar radiation are likely to be a closer representation of reality. The densities at these positions are thus $\sim 10^4 \text{ cm}^{-3}$, which correspond to $N(\text{O}) \sim 10^{19} \text{ cm}^{-2}$ for T_{kin} = 100 K. Most of the observed [O I] 145 μm intensities can be explained by $N(\text{O})$ between $(1\text{--}3) \times 10^{19} \text{ cm}^{-2}$. On the other hand, the column density $N(\text{O})$ of the self-absorbing gas dominating the [O I] 63 μm profile is only one-tenth of the O⁰ column density, which shows up in emission. The total $N(\text{O})$ estimated for the S 1 PDR is similar to the column densities ($> 10^{19} \text{ cm}^{-2}$) seen in dense molecular gas in sources like OMC-1 (Herrmann et al. 1997) and L1689N (Caux et al. 1999). Typical values of $N(\text{O})$ estimated from observations lie between 10^{18} – 10^{19} cm^{-2} (Vastel et al. 2000, 2002).

We estimate the gas pressure to be in the range of 10^4 – 10^8 K cm^{-3} for densities between $10^{3.5}$ – 10^6 cm^{-3} and temperatures, T_{kin}, of 60–120 K in the three gas components we identified. The ambient high density cloud that harbors the ρ Oph A region to the west with typical temperature of 10–20 K and density of 10^6 cm^{-3} (Liseau et al. 2015) has a thermal pressure of around 10^7 cm^{-3} . Although we have detected photoevaporation flows, no streaming motions indicative of large pressure gradient were observed in the PDR and to the west, where it interfaces with the high density molecular cloud. Interestingly, for an assumed temperature of T_{kin} of 100 K, the density of the PDR gas primarily contributing to the thermal pressure and maintaining equilibrium at the interface with the molecular gas, would be 10^5 cm^{-3} . This is consistent with the medium density interclump medium as identified from our analysis of the emission from the PDR gas.

Acknowledgements. The authors would like to thank W. Vacca for his help regarding the stellar type of S 1 and M. Wolfire for allowing the use of the updated PDR models prior to publication. BM acknowledges the support of the Department of Atomic Energy, Government of India, under Project Identification No. RTI 4002. Based on observations made with the NASA/DLR Stratospheric Observatory for Infrared Astronomy (SOFIA). SOFIA is jointly operated by the Universities Space Research Association, Inc. (USRA), under NASA contract NAS2-97001, and the Deutsches SOFIA Institut (DSI) under DLR contract 50 OK 0901 to the University of Stuttgart. The development of GREAT was financed by the participating institutes, by the Federal Ministry of Economics and Technology via the German Space Agency (DLR) under Grants 50 OK 1102,

50 OK 1103 and 50 OK 1104 and within the Collaborative Research Centre 956, sub-projects D2 and D3, funded by the Deutsche Forschungsgemeinschaft (DFG). This research has made use of the VizieR catalog access tool, CDS, Strasbourg, France. The original description of the VizieR service was published in A&AS 143, 23. This research has made use of data from the Herschel Gould Belt survey (HGBS) project (<http://gouldbelt-herschel.cea.fr>). The HGBS is a Herschel Key Programme jointly carried out by SPIRE Specialist Astronomy Group 3 (SAG 3), scientists of several institutes in the PACS Consortium (CEA Saclay, INAF-IFSI Rome and INAF-Arcetri, KU Leuven, MPA Heidelberg), and scientists of the Herschel Science Center (HSC).

References

- Andre, P., Montmerle, T., Feigelson, E. D., et al. 1988, *ApJ*, 335, 940
- André, P., Men'shchikov, A., Bontemps, S., et al. 2010, *A&A*, 518, L102
- Belitsky, V., Lapkin, I., Fredrixon, M., et al. 2018, *A&A*, 612, A23.
doi:10.1051/0004-6361/201731458
- Castelli, F. & Kurucz, R. L. 2003, *Modelling of Stellar Atmospheres*, 210, A20
- Caux, E., Ceccarelli, C., Castets, A., et al. 1999, *A&A*, 347, L1
- Di Francesco, J., André, P., & Myers, P. C. 2004, *ApJ*, 617, 425
- Friesen, R. K., Pineda, J. E., co-PIs, et al. 2017, *ApJ*, 843, 63
- Friesen, R. K., Pon, A., Bourke, T. L., et al. 2018, *ApJ*, 869, 158
- Goldsmith, P. F., Langer, W. D., Pineda, J. L., et al. 2012, *ApJS*, 203, 13
- Goldsmith, P. F. 2019, *ApJ*, 887, 54. doi:10.3847/1538-4357/ab535e
- Güsten, R., Nyman, L. A., Schilke, P., et al. 2006, *A&A*, 454, L13
- Guevara, C., Stutzki, J., Ossenkopf-Okada, V., et al. 2020, *A&A*, 636, A16
- Gupta, Y., Ajithkumar, B., Kale, H. S., et al. 2017, *Current Science*, Vol. 113, 2017, 113, 70
- Gutermuth, R. A., Megeath, S. T., Myers, P. C., et al. 2009, *ApJS*, 184, 18
- Habing, H. J. 1968, *Bull. Astron. Inst. Netherlands*, 19, 421
- Herrmann, F., Madden, S. C., Nikola, T., et al. 1997, *ApJ*, 481, 343
- Hollenbach, D. A., & Tielens, A. G. G. M. 1999 *Rev. of Modern Physics*, 71, 173
- Kaufman, M. J., Wolfire, M. G., Hollenbach, D. J., et al. 1999, *ApJ*, 527, 795
- Kawabe, R., Hara, C., Nakamura, F., et al. 2018, *ApJ*, 866, 141
- Klein, B., Hochgürtel, S., Krämer, I., et al. 2012, *A&A*, 542, L3
- Larsson, B., & Liseau, R. 2017, *A&A*, 608, A133
- Liseau, R., Larsson, B., Lunttila, T., et al. 2015, *A&A*, 578, A131.
doi:10.1051/0004-6361/201525641
- Loren, R. B., Wootten, A., Wilking, B. A. 1990, *ApJ*, 365, 269
- Mookerjea, B., Sandell, G., Vacca, W., et al. 2018, *A&A*, 616, A31
- Mookerjea, B., Sandell, G., Güsten, R., et al. 2019, *A&A*, 626, A131.
doi:10.1051/0004-6361/201935482
- Ortiz-León, G. N., Loinard, L., Kounkel, M. A., et al. 2017, *ApJ*, 834, 141
- Ossenkopf, V., Röllig, M., Neufeld, D. A., et al. 2013, *A&A*, 550, A57.
doi:10.1051/0004-6361/201219837
- Padgett, D. L., Rebull, L. M., Stapelfeldt, K. R., et al. 2008, *ApJ*, 672, 1013
- Pankonin, V., & Walmsley, C. M. 1978, *A&A*, 64, 333
- Purser, S. J. D., Lumsden, S. L., Hoare, M. G., et al. 2016, *MNRAS*, 460, 1039.
doi:10.1093/mnras/stw1027
- Quireza, C., Rood, R. T., Bania, T. M., et al. 2006, *ApJ*, 653, 1226.
doi:10.1086/508803
- Risacher, C., Güsten, R., Stutzki, J., et al. 2018, *Journal of Astronomical Instrumentation*, 7, 1840014. doi:10.1142/S2251171718400147
- Sandell, G., Mookerjea, B., Güsten, R., et al. 2015, *A&A*, 578, A41
- Schmiedecke, A., Schilke, P., Möller, T., et al. 2016, *A&A*, 588, A143
- Stine, P. C., Feigelson, E. D., André, P., et al. 1988, *AJ*, 96, 1394
- Stutzki, J., Stacey, G. J., Genzel, R., et al. 1988, *ApJ*, 332, 379.
doi:10.1086/166663
- Swarup, G., Ananthakrishnan, S., Kapahi, V. K., et al. 1991, *Current Science*, Vol. 60, NO.2/JAN25, P. 95, 1991, 60, 95
- Thompson, R. I. 1984, *ApJ*, 283, 165
- Tielens, A. G. G. M., & Hollenbach, D. 1985, *ApJ*, 291, 722
- van der Tak, F.F. S., Black, J. H., Schoier, F. L., Jansen, D. J., & van Dishoeck, E. F. 2007, *A&A*, 468, 627
- Vastel, C., Caux, E., Ceccarelli, C., et al. 2000, *A&A*, 357, 994
- Vastel, C., Polehampton, E. T., Baluteau, J.-P., et al. 2002, *ApJ*, 581, 315.
doi:10.1086/344136
- White, G. J., Drabek-Mauder, E., Rosolowsky, E., et al. 2015, *MNRAS*, 447, 1996
- Wilson, C. D., Avery, L. D., Fich, M., et al. 1999, *ApJ*, 513, L139
- Wilson, T. L., & Rood, R. 1994, *ARA&A*, 32, 191